Biomass and Bioenergy 154 (2021) 106247

Contents lists available at ScienceDirect

Biomass and Bioenergy

journal homepage: www.elsevier.com/locate/biombioe

Research paper

Numerical and experimental development of integrated electrostatic precipitator concepts for small-scaled biomass furnaces

Florian Schittl [a,*], Lukas Unterpertinger [a], Christian Heschl [b], Jürgen Krail [b]

[a] Forschung Burgenland GmbH, 7423 Pinkafeld, Steinamangerstraße 21, Austria
[b] University of Applied Sciences Burgenland, Department Energy and Environment, 7423 Pinkafeld, Steinamangerstraße 21, Austria

ARTICLE INFO

Keywords:
PM emissions
Electrostatic precipitation
Collection efficiency
CFD
Aerosol measurements

ABSTRACT

Downstream electrostatic precipitators (ESP) represent the state of the art separation technology in medium and large biomass combustion plants. However, these technologies are often difficult to implement in smaller furnaces due to economic aspects and space constraints. This study deals with the integration of ESP systems into the heat exchanger of a small-scale biomass furnace. In order to accelerate the costly and time-consuming development process, preliminary numerical investigations of different ESP configurations were conducted using computational fluid dynamics (CFD). A prototype of the most promising variant were manufactured based on the results of the CFD simulations and experimentally tested with regard to the collection efficiency. In addition to the full load behaviour of the firing system, further test arrangements with several partial-load situations were tested to analyse the particle precipitation under realistic plant conditions with regard to flue gas properties and flow conditions. Furthermore, the collection efficiency for the combustion of different types of biomass was evaluated. Both discontinuous and time-resolved aerosol measuring methods are used to determine particulate matter (PM) emissions. Discontinuous measurements show that at least 55 % of the $PM_{2.5}$ particles are separated with the integrated ESP, both at full and partial load operation of the boiler, irrespective of the fuel used. In the partial load range, collection efficiencies for $PM_{2.5}$ can be increased by up to 75 %, depending on the fuel being fired. In order to enable a more precise observation of the separation behaviour with regard to particle size, additional continuous high-resolution aerosol measurements were carried out for a selected fuel (wood chips w = 20 %). The results show that over 50 % (full load) and over 80 % (part load) of small particles (PM_1) can be separated.

1. Introduction

The increase of the global energy consumption and the associated emission of climate-damaging substances such as carbon dioxide (CO_2) causes a growing demand for renewable and environmental friendly energy resources. Although the thermal utilisation of biomass is not often added to renewable energy resources in its entirety due to the supply chain [1], its expansion and the resulting reduction of fossil fuels contribute significantly to the energy transition process and to climate change mitigation [2].

Nevertheless, particulate emissions are formed during the combustion process of biogenic fuels depending on the type of furnace [3–6], on the operating conditions in terms of combustion quality [7–9] as well as on fuel properties [9–11]. Many studies prove the correlation between these respirable particles and adverse health effects as well as increased mortality rates [12]. Especially the release of submicron particles often leads to health problems such as pulmonary or cardiovascular diseases [13]. Moreover, substances such as polycyclic aromatic hydrocarbons (PAH) accumulate on the surface of these dust or soot particles, which thus also contribute to the additional spread of pollutants as carriers [14]. These organic substances not only have a strong carcinogenic effect on humans, but are also toxic to various environmental organisms.

Due to the large number of negative effects of combustion particles on the environment and health, some European countries have adopted stricter limits for particulate matter (PM) emissions of newly constructed biomass furnaces in recent years. For example, since the beginning of 2011, in Switzerland, total particulate emissions have been legally limited to 40 to 60 $mg\,m_N^{-3}$ (referred to dry exit flue gas, with 13% O_2), depending on the type of biomass furnace [15]. In Germany, much stricter limits for PM emissions have been in force since the 1st BimSchV [16] came into operation in 2015. Specifically, for newly

* Corresponding author.
E-mail address: florian.schittl@forschung-burgenland.at (F. Schittl).

https://doi.org/10.1016/j.biombioe.2021.106247
Received 23 March 2021; Received in revised form 19 August 2021; Accepted 16 September 2021
Available online 28 September 2021

Nomenclature

Latin symbols

$\bar{h}$	Heat transfer coefficient, $W\,m^{-2}\,K^{-1}$
$\dot{m}$	Mass flow rate, $kg\,s^{-1}$
$\dot{Q}$	Heat flux, W
A_d	Ash content, $\%_{db}$
b_I	Gas ion mobility, $m^2\,V^{-1}\,s^{-1}$
c	Mass concentration (solid), $mg\,m^{-3}$
C_D	Drag coefficient, –
c_p	Specific heat capacity, $J\,kg^{-1}\,K$
d	Diameter, m
E	Electric field strength, $V\,m^{-1}$
e	Elementary charge, C
g	Gravitational acceleration, $m\,s^{-2}$
H_o, H_u	Higher and lower heating value, $MJ\,kg_{db}^{-1}$
I	Electric current, A
k	Turbulent kinetic energy, $m^2\,s^{-2}$
k_B	Boltzmann constant, $Wm^{-2}K^{-4}$
l	Length, m
m	Mass, kg
n	Spread parameter, –
P	Electric power, W
p	Pressure, Pa
q	Charge, C
r	Radius, m
S	Energy source term, $W\,m^{-3}$
T	Temperature, K
t	Time, s
U	Voltage, V
u	Velocity, $m\,s^{-1}$
w	Moisture content, $\%_{wb}$
x	Spatial coordinate, m
y	Mass concentration (gaseous), $mg\,m^{-3}$
Re	Relative Reynolds number, –

Greek symbols

α	Surface factor, –
$\bar{\varepsilon}$	Emissivity, –
δ	Relative gas density, –
δ_{ij}	Kronecker delta, –
ϵ_0	Vacuum permittivity, $A\,s\,V^{-1}\,m^{-1}$
ϵ_r	Relative permittivity, –
η	Collection efficiency, –
λ	Thermal conductivity, $W\,m^{-1}\,K^{-1}$
μ	Dynamic viscosity, $kg\,m^{-1}\,s^{-1}$
ϕ	Electric potential, V
ρ	Density, $kg\,m^{-3}$
ρ_I	Ion charge density, $C\,m^{-3}$
ε	Turbulent dissipation rate, $m^2\,s^{-3}$

Subscripts

c	Corona onset
e	Discharge electrode
i	Vector component
ij	Tensor component
P	Particle
0	Standard conditions
‘	Fluctuating component
db	Dry base
f	Fuel
fg	Flue gas
pa	Primary air
ret	Return stream
sa	Secondary air
sup	Supply stream
w	Water
wb	Wet base

Superscripts

max	Maximum
min	Minimum
off	ESP off
on	ESP on

Acronyms

CAD	Computer-aided design
CFD	Computational Fluid Dynamics
DO	Discrete Ordinates
DP	Discrete Phase
ELPI	Electrical Low Pressure Impactor
ESP	Electrostatic precipitator
FMD	Field modified diffusion
NL	Nominal load
PL	Part load
PM	Particulate matter
RANS	Reynolds Averaged Navier Stokes
RKE	Realisable $k-\varepsilon$
SIMPLE	Semi-Implicit Method for Pressure Linked Equations
TSP	Total suspended particles
UDF	User Defined Function
WSGG	Weighted Sum of Grey Gases

installed automatically loaded biomass boilers, dust emissions are limited to $20\,mg\,m_N^{-3}$ (13% O_2). These progressively stricter guidelines regarding the release of dust from combustion processes increasingly require the use of exhaust gas purification systems, even on a smaller scale. One promising possibility for controlling these environmental and health-endangering fine dust particles are electrostatic precipitators (ESP) which are almost exclusively installed as a downstream subsystem due to their design. A detailed discussion regarding different integration possibilities of electrostatic exhaust gas cleaning systems is included in the work of Jaworek et al. [17,18] and Mandl et al. [19], for instance. Preliminary work in this field has focused primarily on dry downstream ESP's. Several studies are dedicated to the optimisation of such separator systems with regard to electrode geometry [20], a rapping process to avoid re-entrainment [21,22] as well as different possibilities for retrofitting in existing combustion plants [23]. Despite numerous studies on the optimisation of ESP's, they are mainly used as an add-on solution in small biomass systems [24–26]. A major drawbacks to exploiting these systems are the space constraints due to the fixed boiler geometry and the comparatively high investment costs involved. This has led authors such as Berhardt et al. [27] to investigate opportunities for the direct integration of such ESP's into the combustion system. The discharge electrode used in the experiments, which is supplied with a high voltage of approximately 30 kV, is built directly into the boiler body (in front of the flue gas outlet) of a 50 kW wood chip furnace. Depending on the fuel, overall separation efficiencies of about 89% (wood chips, $w = 40\%$) and 72% (wood briquettes) were achieved, respectively. A similar approach towards ESP implementation is proposed in the work of Kelz et al. [28]. The object of the study was a 50 kW biomass boiler, specially designed for varying fuels, where the discharge electrode is installed directly into the second flue gas heat exchanger. Three different fuels (soft wood pellets, poplar wood chips and maize spindle grits) are investigated in terms of PM precipitation by discontinuous gravimetric measurements as well as time-resolved measurements using an electrical low pressure impactor (ELPI). At nominal operation conditions, collection efficiencies between 68% (pellets) and 90% (wood chips) are reached for particles smaller than 1 μm, while at partial load between 68% (maize spindle) and 85% (pellets) of PM_1 emissions can be captured. Molchanov et al. [29] take a further step towards integrated ESP's. In their work, two discharge electrodes with several side-attached discharge wires are positioned in front of the flue gas outlet of a 15 kW boiler. The collection efficiency of the ESP, which is supplied with a voltage of 20 kV, is found by ELPI as well as gravimetric measurements. The resulting reduction of PM emissions is about 56% at nominal load and 67% at partial load. Blank et al. [30] carry out both, experimental and numerical investigations regarding the effect of an ESP in a 26 kW pellet combustion plant. The sawtooth-shaped discharge electrode is situated centrally in the flue gas pipe after the ash container and supplied with a high voltage of about 15 kV. The observed collection efficiency for the PM_1 fraction is determined using a low-pressure Berner-type impactor and ranges from 86.5% (nominal load) to 91.5% (part load). The 3D-CFD simulations were performed with the commercial finite volume code ANSYS Fluent and are in good agreement with the experimental data.

However, increasing computing capacities in the last decades can influence the development process of such separator technologies already before the production of a prototype as well as optimise the system configuration if necessary. Numerical methods like computational fluid dynamics (CFD) are frequently used to illustrate the interactions between flue gas flow field and particle motion [31–34]. In [35] the authors investigated the operation of a wire-plate ESP with the use of the commercial CFD code ANSYS Fluent. Using the UDF (User defined function) interface, the model structure was extended by the full electrostatic field equations, where the electric current density is composed of conduction, convection and diffusion effects. The model was applied to a 2D ESP geometry as well as to different furnace operating conditions. The calculations showed that an increase in supply voltage or a decrease in inlet velocity is required to improve collection efficiency, especially for small particles. Dastoori et al. [36] used the finite element based software package COMSOL Multiphysics to investigate an ESP in the vertical chimney of a biomass fired stove. Similar to the study mentioned above, the balance equations for mass and momentum are coupled with the electrostatic field equations, with the difference that the conduction term in the charge conservation equation is neglected. Furthermore, a simplified model approach for the particle charging mechanism is used. The results for the investigated ESP configuration showed that beside the voltage, the length of the discharge electrode is crucial. Furthermore, it could be shown that the ionic wind creates small eddies near the surfaces and thus deteriorates the deposition of small particles. It can be deduced from the trajectories of the particles that the insertion of grounded baffles minimises these effects and thus improves collection efficiency. Arif et al. [37] presents a combined approach to calculate electrohydrodynamic flow conditions as well as particle movement around a discharge electrode. The freely available software OpenFOAM is used for computing the electrostatic field quantities such as electric potential or ion charge density, while subsequent flow simulation and particle tracking is performed with the commercial CFD code STAR-CCM+. This methodology allows an evaluation of particle charging as a function of position relative to the discharge electrodes and thus creates an accurate and effective framework to investigate ESP's. Since there are a large number of different software solutions available for the numerical investigation and optimisation of ESP's, Bhasker [38] compares four different program solutions. The CFD solvers are analysed in terms of performance and accuracy using the example of ESP ducts with turning vanes. The study shows that the commercial CFD code ANSYS Fluent achieves quick and sufficiently accurate results and is thus ideally suited for the industrial development process. It can already be concluded that CFD simulations are a proven tool in the development process of integrated ESP's.

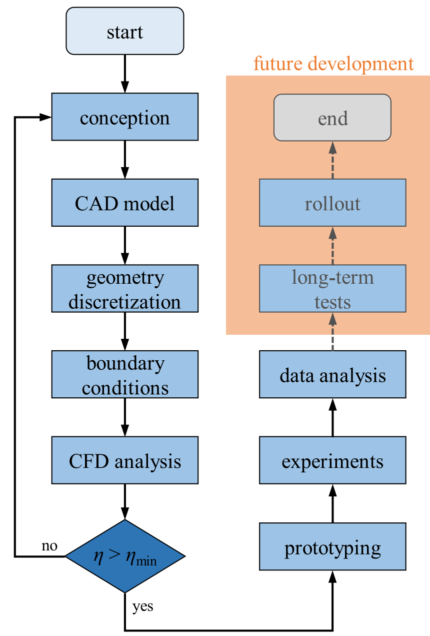

Fig. 1. Flow diagram for the development process of integrated ESP's in small-scaled biomass furnaces.

2. Materials and methods

2.1. Development process

The use of ESP's is one of the most promising options for reducing PM emissions through secondary measures, particularly in terms of cost, efficiency and reliability. This technology is already widely used as a separate module for retrofitting, especially for small biomass furnaces. However, separating the ESP from the boiler entails operational disadvantages in terms of higher costs and space requirements. For these reasons, this study proposes a concept that integrates the ESP directly into the boiler body. The discharge electrode supplied with a high voltage module is positioned after the first flue gas heat exchanger in the lower reversing chamber, which is modified accordingly. The basic electrode geometry is made up of plate electrodes formed from two curved sheets of metal. Care must be taken when arranging the discharge electrodes to avoid frequent spark discharges to the grounded boiler walls in order to ensure continuous operation and efficient electrostatic charging of the particles. The grounded heat exchanger surfaces after the reversing chamber act as a collection electrode. The control for the power supply as well as the measurement data acquisition is implemented via a ModBUS protocol into the existing LabVIEW® program of the biomass boiler test rig.

The sequence of the development process for the integration of the ESP into the existing biomass furnace is shown in Fig. 1 and starts with the design procedures. First of all, the geometry of the existing combustion plant is mapped using a CAD model, before the mounting position is determined on the basis of an assumed supply voltage and the associated minimum distances to the boiler walls. After the completion of the digital prototype, the computational domain is discretised by the finite volume method. After setting the appropriate boundary conditions, numerical simulations of the electrohydrodynamic flow conditions as well as the particle movement around the ESP (see Section 2.3) are carried out using ANSYS Fluent. Based on the results of the CFD simulation, theoretical considerations regarding possible optimisation measures are conducted to reduce the time required for the development process. For the analysis of the ESP performance, conventional post-processing methods such as streamlines as well as the visualisation of the particle trajectories by means of Lagrangian particle tracking are used. If the calculated collection efficiency meets the minimum requirements ($\eta > \eta_{\min}$), the prototype phase starts and the construction of the most promising version takes place. Otherwise, the process branches off into the feedback-loop, where the separator setup is changed until an improvement in particle separation can be detected. The main parameters to be considered in the optimisation procedure of ESP are the supply voltage U, the electrode geometry l_e and the flow conditions around the electrode. After the fabrication of the ESP and its installation in the boiler body, aerosol emissions are measured as described in Section 2.4. In the course of the measurement data analysis, various influences on the collection efficiency such as different fuels or operating state of the furnace are investigated and compared against the simulation results. Long-term or field measurements for the evaluation of the operational fitness as well as the degradation resistance of ESP are considered as future development steps and will not be discussed in this paper. The same applies to the preparation of test certificates, which are necessary for the final step which namely is the market introduction.

2.2. Test bench and integration concept

The investigated system is a small grate combustion furnace, as it is commonly used in the small capacity range, e. g. for residential facilities, and illustrated in Fig. 2. Basically, the boiler is designed for the combustion of wood pellets or wood chips, although operation with other types of fuel is also possible, as long as the fuel is provided in small pieces by the conveyor system. The controlled variables of the boiler system are the wet fuel mass flow $\dot{m}_{\mathrm{f}}$, the primary air mass flow $\dot{m}_{\mathrm{pa}}$ and the secondary air mass flow $\dot{m}_{\mathrm{sa}}$, whereby the latter is divided. The air flow $\dot{m}_{\mathrm{sa1}}$ is brought into the free space directly above the grate, while $\dot{m}_{\mathrm{sa2}}$ corresponds to the air flow that supports complete combustion in the freeboard. However, the air mass flows cannot be controlled independently in the basic version of the boiler. All three mass flows depend on the speed of the single fan in the exhaust system that draws the air through the boiler. The secondary air mass flow $\dot{m}_{\mathrm{sa2}}$ can be adjusted by an additional valve that allows $\dot{m}_{\mathrm{sa2}}$ to be almost completely shut off. However, the geometric conditions of the flow system allow for an explicitly constant ratio between $\dot{m}_{\mathrm{pa}}$ and $\dot{m}_{\mathrm{sa1}}$, which is normally set during installation of the furnace. This ratio contains empirical fuel-specific knowledge for the air mass flows and requires manual adjustment for different fuel types due to the existing PI feed-forward control.

The water mass flow $\dot{m}_{\mathrm{w}}$ of the heating circuit enters a two-part heat exchanger with the return water temperature T_{ret}, is continuously heated by the hot flue gas and leaves the furnace with the feed water temperature T_{sup} on the warmer heat exchanger side. The span between these two temperatures is the main measure of the energy supplied by the boiler to the heating circuit. In the examined system, the water mass flow $\dot{m}_{\mathrm{w}}$ and the return temperature T_{ret} are kept constant on the test bench in order to be able to ensure constant boundary conditions for the evaluation of the collection efficiency.

The ESP is integrated into the biomass furnace taking into account the given boiler geometry, as can be seen in Fig. 2. The discharge electrode including the insulator is placed in the boiler body, after the first heat exchanger section in the centre of the lower reversing chamber. The surrounding metal surfaces of the boiler wall or the subsequent heat exchanger surfaces act as the collecting electrode. The discharge electrode is composed of two pairs of plates, each consisting of two curved metallic sheets. The two sheets are about 2.3 cm wide and vary in length depending on the ESP variant. The electrode is powered by a high-voltage module that supplies between 15 and 40 kV and is linked to the existing visualisation system for monitoring purposes.

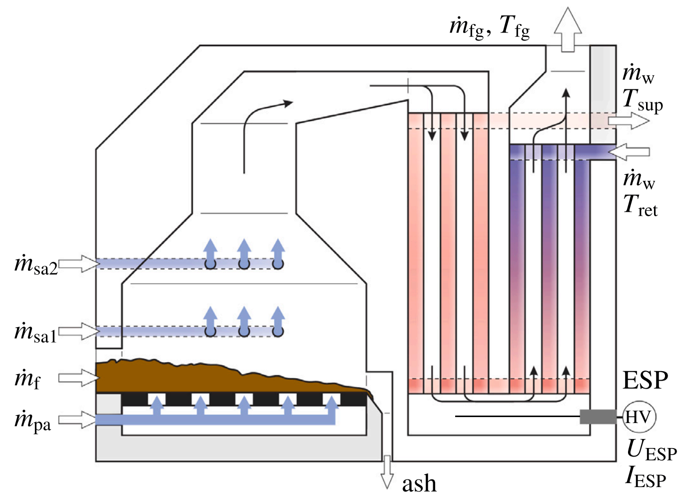

Fig. 2. Schematic representation of the investigated biomass boiler with integrated ESP.

2.3. Numerical computations

2.3.1. Governing equations

The numerical investigation of ESP's requires a variety of models and methods which are summarised in Table 1. The simulation of the flue gas flow around the ESP is based on the conservation laws of continuum mechanics. The conservation of mass and momentum can be described by the incompressible three-dimensional stationary Reynolds Averaged Navier–Stokes (RANS) equations (equation (1) and (2)). The influence of electrostatic field forces is considered by an additional source term in the momentum equation and can be calculated as a function of ion charge density ρ_I and electric field strength E_i. Eq. (3) represents the conservation of thermal energy, whereby this balance equation can be expressed by a transport equation for temperature using some simplifications.

$$\frac{\partial}{\partial x_i}\left(\rho u_i\right) = 0 \tag{1}$$

$$\frac{\partial}{\partial x_j}\left(\rho u_i u_j\right) = -\frac{\partial p}{\partial x_i} + \frac{\partial}{\partial x_j}\left[\mu\left(\frac{\partial u_i}{\partial x_j} + \frac{\partial u_j}{\partial x_i} - \frac{2}{3}\delta_{ij}\frac{\partial u_k}{\partial x_k}\right)\right] + \frac{\partial}{\partial x_j}\left(-\rho\overline{u_i' u_j'}\right) + \rho g_i + \rho_I E_i \tag{2}$$

$$\frac{\partial}{\partial x_i}\left(\rho c_p u_i T\right) = \frac{\partial}{\partial x_i}\left(\lambda\frac{\partial T}{\partial x_i}\right) + \frac{\partial}{\partial x_i}\left(-\rho\overline{u_i' T'}\right) + S \tag{3}$$

In addition to the above mentioned model equations for the fluid flow and the heat transfer mechanism, further model approaches are required for the closure or refinement of the problem. Nitrogen (N_2), carbon dioxide (CO_2), oxygen (O_2) and water vapour (H_2O) represent the four main components of the exhaust gas stream, which can therefore be modelled in good approximation by the ideal gas law. Consequently, the pressure p is coupled with the mean flue gas density ρ and the temperature T via the thermal equation of state. The thermophysical properties of the gas are determined as a function of temperature. The turbulent fluctuations of the gas flow are modelled using the Realisable $k-\varepsilon$ eddy viscosity model (RKE) proposed by Shih et al. [39]. The standard wall function approach is used to reproduce

Table 1
Solver setup and model configuration for the CFD simulation of the flue gas flow, heat and particle transport.

Problem	Model approach
Mass/momentum exchange	3D steady RANS equations
Equation of state	Ideal gas law (incompressible)
Turbulence	RKE model with wall functions
Particle transport	DP model
Particle charging	FMD model
Heat radiation	DO model
Gas radiation properties	WSGG model
Pressure velocity coupling	SIMPLE algorithm

the flow in cells close to walls [40]. The discrete ordinates model (DO) is used to consider the effects of thermal radiation emanating from the boiler walls, as both accuracy and calculation effort have proven to be effective for these applications [41]. The attenuation of the heat radiation intensity by the gas molecules within the biomass furnace is modelled using the weighted sum of grey gas model (WSGG). Furthermore, the SIMPLE algorithm developed by Patankar [42] is used for pressure velocity coupling.

As can be seen from the set of partial differential equations, further transport variables are necessary to model electrohydrodynamic flows. Starting from the time-independent Maxwell equations, a simplified decoupled system of equations can be derived under the assumption of (i) negligibly small magnetic field strengths, (ii) diluted flows ($\rho_I \gg \rho_P$), and (iii) disappearing low diffusion and convection effects of the ions. A quasi-static electric field can therefore be described by a Poisson equation (4), where ϕ refers to the electric potential and ϵ_0 to the vacuum permittivity. The electric field strength required for the momentum equation can be calculated by applying the gradient operator to the scalar field, $E_i = -\partial\phi/\partial x_i$. The source of the electric field is defined as the space charge density ρ_I, which indicates the conservation of charge. If it is assumed that the space charge only influences the strength and not the direction of E_i, the transport equation for ion transport is transformed into a quasi-linear weighted differential equation (5) [43,44].

$$\frac{\partial^2\phi}{\partial x_i^2} = -\frac{\rho_I}{\epsilon_0} \tag{4}$$

$$E_i\frac{\partial\rho_I}{\partial x_i} = -\frac{\rho_I^2}{\epsilon_0} \tag{5}$$

The disperse phase is considered in a lagrangian reference system and modelled using the Discrete Phase (DP) model. The motion of a representative particle collective through the flow field can be obtained by solving the time-dependent ordinary differential equation for the particle position $x_{P,i}$ and the particle velocity $u_{P,i}$, respectively. The acceleration due to the virtual mass and the Basset force can be neglected for very small particles. Furthermore, the Saffman lift force can also be omitted due to its particle size dependence. In addition, the effect of the Brownian motion is also taken into account. Consequently, Eq. (6) for particle motion is reduced to the inertia, drag and electrostatic forces. [45]

$$\frac{\mathrm{d}^2x_{P,i}}{\mathrm{d}t^2} = \frac{3\mu C_D\mathrm{Re}}{4\rho_P d_P^2}\left(u_i - u_{P,i}\right) + \frac{g_i\left(\rho_P-\rho\right)}{\rho_P} + \frac{E_i q_P}{m_P} \tag{6}$$

The calculation of the drag coefficient is based on the correlation published by Rowe and Henwood [46], where C_D can be determined as a function of the relative particle Reynolds number $\mathrm{Re} = \rho d_P|u_{P,i} - u_i|/\mu$. Furthermore, the fact of reduced particle adhesion to surfaces is supported by the use of the so-called Cummingham correction [47]. Although weight and buoyancy forces have little influence on particles smaller than 10 µm, these forces are taken into account in the simulations using Archimedes' principle. In the case of particle separation using ESP, however, the driving force originates from the interaction between the electrostatic field and the disperse phase. This force can be represented by a linear dependence on the particle charge. After summing up all forces, the particle trajectory can be determined by calculating the next particle location $x_{P,i}$ after a time step dt.

The charging characteristics of particles in an electrostatic field is essentially driven by two mechanisms, namely field charging, which is mainly relevant for large particles as well as diffusion charging for small particles. The consideration of both mechanisms requires the solution of another differential equation which leads to a high numerical effort for the majority of particle charging models [43]. According to the numerical investigations performed by Long and Yao [48], who evaluated the accuracy of different particle charging models, the field modified diffusion model (FMD) developed by Lawless [49] is most suitable for modelling charging kinetics in ESP's. This model approach accounts for both mechanisms, using the saturation charge $q_P^{\max}$ which is typically expressed in terms of the particle diameter d_P and the electric field intensity $|E_i|$ and defined in Eq. (7) as a decision criterion. [50]

$$q_P^{\max} = 3\pi\epsilon_0 d_P^2\frac{\epsilon_{r,P}}{\epsilon_{r,P}+2}|E_i| \tag{7}$$

As long as the particle charge is lower than the saturation charge, both field and diffusion charging are considered. Accordingly, the charging current for $q_P \le q_P^{\max}$ is composed of two terms, where the field charge is dominant. If the particle charge exceeds the saturation charge ($q_P > q_P^{\max}$), the charging current is reduced as only diffusion charging is effective. The linear differential equation for the charging current thus assumes the following mathematical form

$$\frac{\mathrm{d}q_P}{\mathrm{d}t} = \begin{cases} \dfrac{\rho_I b_I q_P^{\max}}{4\epsilon_0}\left(1-\dfrac{q_P}{q_P^{\max}}\right)^2 + \dfrac{2\alpha(\tilde{E})\pi\rho_I b_I k_B T d_P}{e} & \text{for} \quad q_P \le q_P^{\max} \\ \dfrac{\alpha(\tilde{E})\rho_I b_I\left(q_P - q_P^{\max}\right)}{\epsilon_0\exp\left[\dfrac{e\left(q_P-q_P^{\max}\right)}{2\pi\epsilon_0 k_B T d_P}-1\right]} & \text{for} \quad q_P > q_P^{\max} \end{cases} \tag{8}$$

where T refers to the temperature, k_B to the Boltzmann constant, b_I to the gas ion mobility and e to the elementary charge. The quantities ϵ_0 and $\epsilon_{r,P}$ refer to the vacuum permittivity and the dielectric constant of the particle, respectively. Furthermore, a surface factor $\alpha(\tilde{E})$ which defines the effective particle surface for the diffusion charge is introduced. Inhomogeneous ion concentrations, which are caused for example by high field strengths or low temperatures, are considered by using this factor. As can be seen from the definition equation, the surface factor decreases with an increase in this inhomogeneity. In the case of small particles or low electric field strengths, $\alpha(\tilde{E})$ equals 1, which means that the entire particle surface is available for charging. The surface factor can be calculated by Eq. (9), where the dimensionless field strength $\tilde{E}$ is equal to $d_P e|E_i|/(2k_B T)$.

$$\alpha(\tilde{E}) = \begin{cases} \dfrac{1}{\left(\tilde{E}+0.457\right)^{0.575}} & \text{for} \quad \tilde{E} \ge 0.525 \\ 1 & \text{for} \quad \tilde{E} < 0.525 \end{cases} \tag{9}$$

2.3.2. Numerical grid

The numerical calculation of flow and particle transport processes using the finite volume method requires a spatial discretisation of the calculation domain. The spatial discretisation of the experimental object explained in Section 2.2 is carried out by different sub-grids, according to which both structured and unstructured cell elements are considered. The reason for this subdivision is the complex geometry of the flow region. The heat exchanger inlet as well as the subsequent heat exchanger tubes are represented by a structured grid, which remains unchanged in all variants. The complex curved contours of the turbulators, which serve to clean the heat exchanger, do not allow an exactly regular grid, so increased values for skewness must be expected for these cells. In order to guarantee an acceptable calculation

Table 2
Boundary conditions for the CFD simulation in terms of flue gas flow, heat transport, particle motion as well as the electrostatic field quantities.

Face	Mass & momentum	Species (N_2, CO_2, O_2, H_2O)	Energy	Electric potential	Ion charge density	Particle
Heat exchanger inlet	$0.07\,\mathrm{kg\,s^{-1}}$	67.2, 18.8, 7.93, 5.99 $\%_{\mathrm{wb}}$	713 °C	$\partial\phi/\partial x_i = 0$	$\partial\rho_I/\partial x_i = 0$	Reflect
Heat exchanger outlet	–	–	–	$\partial\phi/\partial x_i = 0$	$\partial\rho_I/\partial x_i = 0$	Escape
Heat exchanger surface	$0\,\mathrm{m\,s^{-1}}$	–	$\dot{Q} = \bar{h}\partial T/\partial x_i$	0 V	$\partial\rho_I/\partial x_i = 0$	Reflect/trap
Reversing chamber surface	$0\,\mathrm{m\,s^{-1}}$	–	$\partial T/\partial x_i = 0$	0 V	$\partial\rho_I/\partial x_i = 0$	Trap
Discharge electrode	$0\,\mathrm{m\,s^{-1}}$	–	$\partial T/\partial x_i = 0$	ϕ_0	Eq. (11)	Reflect
Isolating surfaces	$0\,\mathrm{m\,s^{-1}}$	–	$\partial T/\partial x_i = 0$	$\partial\phi/\partial x_i = 0$	$\partial\rho_I/\partial x_i = 0$	Reflect

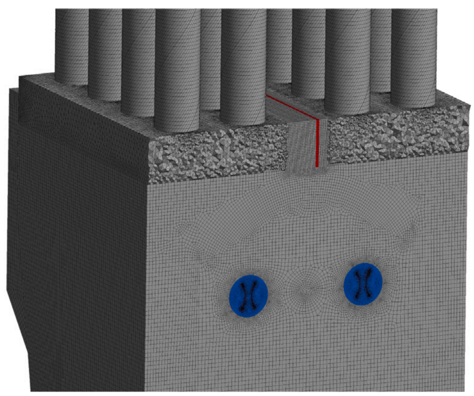

Fig. 3. Three-dimensional finite volume grid for the numerical investigation of the integrated ESP (Var3). The total number of cells lies between 12 372 414 and 13 927 246, depending on the ESP variant. (For interpretation of the references to colour in this figure legend, the reader is referred to the web version of this article.)

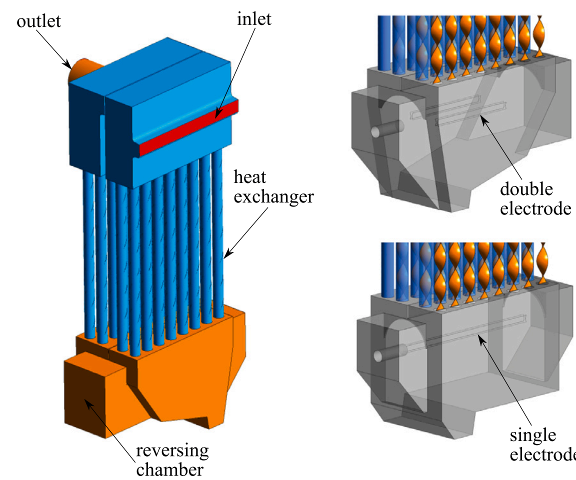

Fig. 4. Representation of the heat exchanger geometry of the biomass furnace and its subdivision into different boundary faces. The two different configurations of the discharge electrode are placed in the reversing chamber after the first heat exchanger section.

time, a detailed resolution of the boundary layer with the help of inflation layers is omitted, since this region is modelled with the help of wall functions anyway. The average dimensionless wall distance of the individual grid variants is approximately 11. The grid generation in the reversing chamber, which is shown schematically for variant 3 in Fig. 3, is also based on a grid of regular hexahedral elements. Critical regions in this subgrid are the baffle element (marked red) as well as the cylindrical volume elements around the discharge electrodes (blue). Since the latter subgrid is essential for modelling the electric field forces, the cells are resolved more refined here. The upper subgrid of the reversing chamber, which acts as a connection to the heat exchanger grid, is formed by an irregular grid consisting of tetrahedral elements. The associated loss of quality with regard to partially high aspect ratios is accepted here, as this ensures a smooth and gap-free transition between the individual grid segments.

To assess the grid quality, criteria such as the skewness are used. According to the specifications of the CFD solver ANSYS Fluent, the skewness for the majority of the cells in the calculation domain should be between 0 and 0.5 and should not exceed a value of 0.95. Since the considered meshes consist mostly of block-structured hexahedral elements, low values for the skewness of the cells (the maximum values are about 0.23) can be achieved. Another characteristic for the qualitative assessment of a FVM grid is the so-called aspect ratio. In general, the aspect ratio should be between 1 and < 10. Aspect ratios of an average of 3.2 and a maximum of 3.8 can be achieved for the investigated grid variants.

2.3.3. Boundary conditions

For the execution of the numerical simulations and the associated solution of the transport equations mentioned in the previous section, corresponding geometrical as well as physical limits of the transport quantities must be set at the edges of the computational domain. These boundary conditions for the different faces of the boiler geometry and the electrode surface are summarised in Table 2 (see Fig. 4).

The entry into the boiler geometry is defined as velocity inlet and given by the previously measured exhaust gas mass flow rate

Table 3
Entrance boundary conditions for Lagrangian particle tracking as well as the properties of the different dust fractions [30,51].

Type	$\dot{m}_P$ $\mathrm{kg\,s^{-1}}$	ρ_P $\mathrm{kg\,m^{-3}}$	$\epsilon_{r,P}$ –	$d_P^{\min}$ µm	$d_P^{\max}$ µm	$\bar{d}_P$ µm	n –
Soot	$3.87\cdot10^{-9}$	1700	19	0.025	1.4	0.16	1.44
Salt	$5.74\cdot10^{-8}$	2300	5	0.025	5.5	1.15	0.52
Tar	$7.60\cdot10^{-9}$	1100	4	0.025	5.5	1.15	0.52
Coarse fly ash	$7.44\cdot10^{-8}$	2500	5	6	25	16.83	4.12

and the corresponding cross-sectional area. Furthermore, the average temperature T measured in the combustion chamber is imprinted at the inlet. Previous measurements are also used to determine the species distribution of the main exhaust gas components at the inlet. A pressure outlet boundary condition is applied to the exhaust gas outlet. The approximation of the turbulence parameters k and ε at the open ends is made by estimating the turbulent intensity and a turbulent length scale. These quantities can be calculated for a fully developed turbulent flow as a function of Reynolds number and characteristic length. The logarithmic Rosin–Rammler distribution is used to provide a particle collective consisting of soot, tar, salts as well as coarse fly ash at the heat exchanger inlet. In addition to the corresponding limits regarding the particle diameters ($d_P^{\min}$ and $d_P^{\max}$), a mean diameter $\bar{d}_P$ and a spread parameter n must be specified for each particle type. The values for these parameters can be calculated based on the measured mass distributions of the respective dust constituents given in [51] (see Table 3). Furthermore, a so-called escape boundary condition is set at the outlet in order to determine the collection efficiency of the ESP.

To characterise the momentum transport near solid walls, the no-slip boundary condition ($u = 0$) is used. All surfaces except the heat exchanger are considered as adiabatic, $\partial T/\partial x_i = 0$. The heat transfer between flue gas and heat exchanger surface is calculated using a mean emissivity $\bar{\varepsilon}$ of 0.9 and a mean heat transfer coefficient $\bar{h}$ of $1000\,\mathrm{W\,m^{-2}\,K^{-1}}$. The electric potential at both the discharge electrode

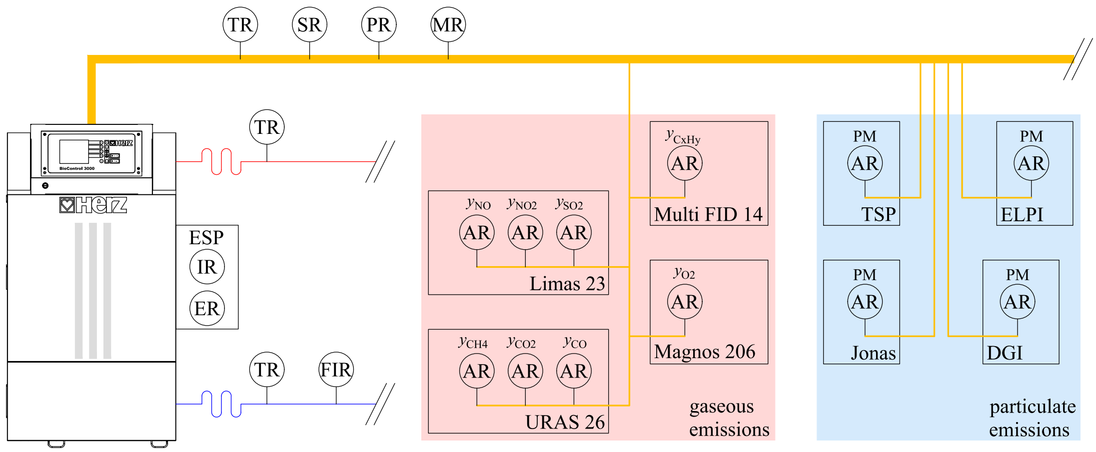

Fig. 5. Experimental set-up for the evaluation of emissions from biomass furnaces. The composition of the flue gas is continuously determined by extractive gas analysers, while the dust load is measured either continuously by the ELPI or discontinuously by the cascade impactors.

and the collection electrode is given by a Dirichlet boundary condition. Accordingly, a potential difference in the height of the voltage ϕ_0 at the operating point of the ESP is established between these two surfaces. At isolating surfaces a zero-gradient boundary condition for the scalar quantity ϕ applies analogous to the entrance and the exit faces. For the second electrostatic field quantity, $\partial \rho_I / \partial x_i = 0$ applies to all surfaces of the computational domain except the discharge electrode. However, for the surrounding environment of the discharge electrode a fixed value of the space charge density is required to obtain the electrohydrodynamic coupling. It is assumed that the field strength on the corona edge does not change after exceeding the corona onset voltage until the breakdown voltage is reached [52]. The field strength at the corona onset E_c can be estimated according to the empirical approach of Peek [53]

$$E_c = 3 \cdot 10^6 \left(1 + 0.03 \sqrt{\frac{\delta}{r_e}}\right) \tag{10}$$

where $\delta = T_0 p/(T p_0)$ denotes the relative gas density and r_e the wire radius. Although this equation assumes a cylindrical geometry of the discharge wire and is therefore not valid for the ESP configuration, it provides a good initial guess for the space charge density at the discharge electrode. An iterative adjustment of ρ_I is performed until the electric field strength magnitude $|E_i|$ corresponds to the corona onset field strength E_c. [54]

$$\rho_I \left(E_0\right) = \frac{I_c}{2\pi r_e l_e b_I E_c} \tag{11}$$

In addition to geometric parameters such as the radius r_e or the length l_e of the discharge electrode, Eq. (11) also includes the estimated operating current I from the current–voltage characteristic curve of the ESP configuration.

For the evaluation of the collection efficiency, a trapping condition is specified on the heat exchanger surfaces as well as on the walls of the reversing chamber. A reflection condition is specified at the remaining electrically non-conductive surfaces and for the discharge electrode. The reflection depends on the normal and tangential reflection parameter, which are both set to a constant value of 0.25.

2.4. Experimental techniques

The entire measuring set-up used for the investigations consists of a large number of sensors as well as various measuring instruments for analysing the exhaust gas and is shown in a simplified form in Fig. 5. Recording the temperatures and mass flow rate is required for the determination of the boiler heat output. Furthermore, extractive gas analysers (NDIR, NDUV, FID and paramagnetic oxygen sensor) are used to determine the exhaust gas composition. Data management and acquisition was performed by the commercial software package LabVIEW®.

The aerosol sampling methods by the three-stage Jonas cascade impactor (Co. Paul Gothe GmbH) as well as with the four-stage DGI (Dekati Gravimetric Impactor, Co. Dekati Ltd.) are based on inertial forces acting differently on particles of different sizes. The separation diameters can be quantified as 2.5/10.0 μm and 0.2/0.5/1.0/2.5 μm, respectively. The impactor consists of a sampling probe, the inlet cone, the individual impactor nozzles, the plane quartz filters and trace heating, that prevents the condensation of water vapour contained in the exhaust gas. Furthermore, both impactors are equipped with a back-up filter in which the remaining particles are retained after the last stage. The gravimetric impactor measurements are carried out in accordance with the VDI 2066 guideline [55], where a partial volume flow of the flue gas is extracted under isokinetic conditions. Supplementary, a cyclone is installed upstream the DGI apparatus in order to pre-separate coarse particles. The temperature and humidity level of the sampled exhaust gas is reduced by a water-cooled heat exchanger and a silica gel container after passing through the impactor. Subsequently, the actual nominal volume flow is obtained using a diaphragm gas meter. After the filters have been conditioned appropriately in an oven and a desiccator, the particle load per stage can be determined by the difference of the weight difference of the quartz filters, measured before and after the dust sampling. The dry nominal particle concentration $c(d_P)$ can then be calculated by dividing the mass difference of the filters by the exhaust flue gas volume. The estimation of measurement uncertainty is based on the calculation rules suggested by Schröder et al. [56]. In addition to isokinetic sampling conditions, the precision of the weight measurement of the filters is regarded as a decisive factor for measurement inaccuracy [57].

The continuous determination of the PM emissions is carried out by using an electrical low-pressure impactor (ELPI) from the Co. Dekati Ltd. [58]. Similarly to the gravimetric impactor measurements, a partial stream is taken from the flue gas and subsequently diluted with the aid of two mixers connected in series. The functional principle of the mixers is based on the ejection dilution, according to which compressed air causes a pressure drop around a nozzle and thus diluting the extracted flue gas. The ELPI has a total of 12 impactor stages with cut-off diameters between 0.04 and 9.24 μm and uses the same separation principle as the gravimetric impactors, except that the particles are electrically charged before entering the impactor. After that, the charged particles release their charge at the stage where they are deposited. The particle size distribution is calculated based on the resulting current signal. To obtain a mass-related particle concentration, a correction factor for the density and shape of the particles is computed. Due to the heterogeneity of the particles it is not possible to determine reliable correction factors by theoretical calculations. Therefore, further data in terms of particle load (e. g. gravimetric measurements) are necessary to generate an average correction factor. The exact calculation procedures for the calibration of the ELPI signal are given for example in Marjamäki et al. [59].

3. Results

3.1. Numerical results

In this section, the improvement potentials for particle separation that have been identified with the help of CFD simulations are explained. First, the positioning of the electrode is examined based on velocity distributions inside the reversing chamber before the charging of the particles is optimised by varying the supply voltage U as well as the electrode geometry. The following design variants of the ESP result from the development process described in Section 2.1.

- Variant 1: single electrode ($U = 22.8\,\mathrm{kV}$; $I = 45\,\mu\mathrm{A}$)
- Variant 2: single electrode ($U = 28.0\,\mathrm{kV}$; $I = 200\,\mu\mathrm{A}$)
- Variant 3: double electrode ($U = 28.0\,\mathrm{kV}$; $I = 800\,\mu\mathrm{A}$)

3.1.1. Flow field simulation

The first step when integrating the ESP is to find the right position for the discharge electrode in the boiler body. Since the installation options for direct integration are limited anyway by the heat exchanger geometry of the boiler, this position is determined on the basis of fluid mechanical criteria such as flow velocity [60] or gas temperature [61]. These parameters are investigated with the help of a simple CFD model, which does not take the electrostatic field forces into account at this stage. The calculated velocity distributions show that the highest flue gas velocity of over $8\,\mathrm{m\,s^{-1}}$ in the heat exchanger tubes can be reduced to well below $3\,\mathrm{m\,s^{-1}}$ in the lower reversing chamber. Observing the streamlines in this area instead of the averaged velocity field (Fig. 6, a), it can be seen that they are far apart in certain areas, resulting in a homogeneous vortex roll over the entire reversing chamber. The dust particles transported with the fluid consequently migrate along the boiler wall until they enter the second heat exchanger and hinders a targeted and efficient particle charging, due to the distance to the discharge electrode. The second problem that becomes apparent when observing the streamlines is the short-circuited flow between the two inner heat exchanger tubes. Although the particles on these streamlines are in the right zone for efficient charging, there is a risk that the high inlet momentum combined with short residence times will also lead to insufficient separation of the particles. One way to counteract these two effects is the placement of baffles directly at the transition to the flue gas heat exchanger (see Fig. 6, b). A comparison of the flow patterns of the two cases shows that in the variant with baffle plates, the streamlines in the middle area of the reversing chamber are significantly condensed. The additionally applied resistance and the resulting increased turbulence intensity cause an amplified vortex formation around the discharge electrode, which in turn results in an increased residence time of the particles. Furthermore, the baffles prevent the formation of the previously mentioned rolling movement of the flue gas flow and thus reduce the effect of the short-circuit flow. This modification makes it possible to optimise the flow conditions in the reversing chamber and thus forms the basis for the integration of the ESP.

3.1.2. Electrostatic field simulation

In addition to the hydrodynamic flow conditions, the electrostatic field quantities are also of substantial importance for the investigation or optimisation of the ESP. Besides the electric potential ϕ and its spatial derivative E_i, the analysis of the electrostatic field mainly relies on the scalar quantity ρ_I which describes the conservation of charge. As can be seen from the model approaches explained in Section 2.3, the

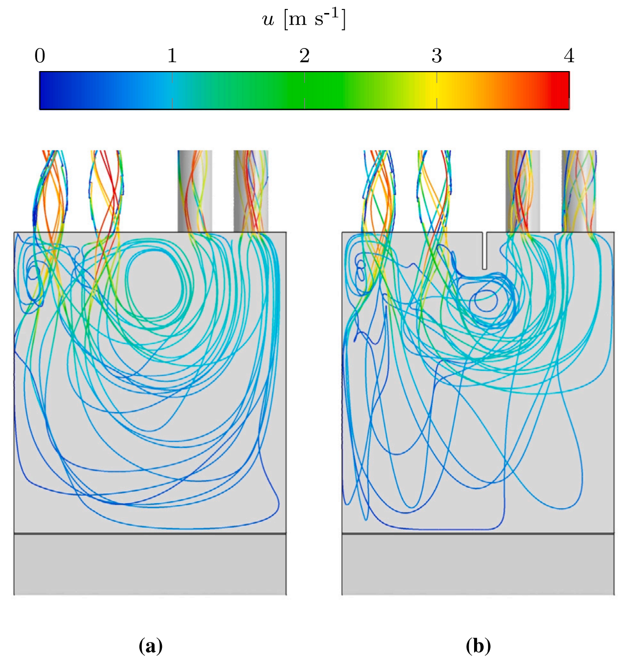

Fig. 6. Calculated path of the streamlines in the reversing chamber of the biomass furnace (a) without and (b) with baffle.

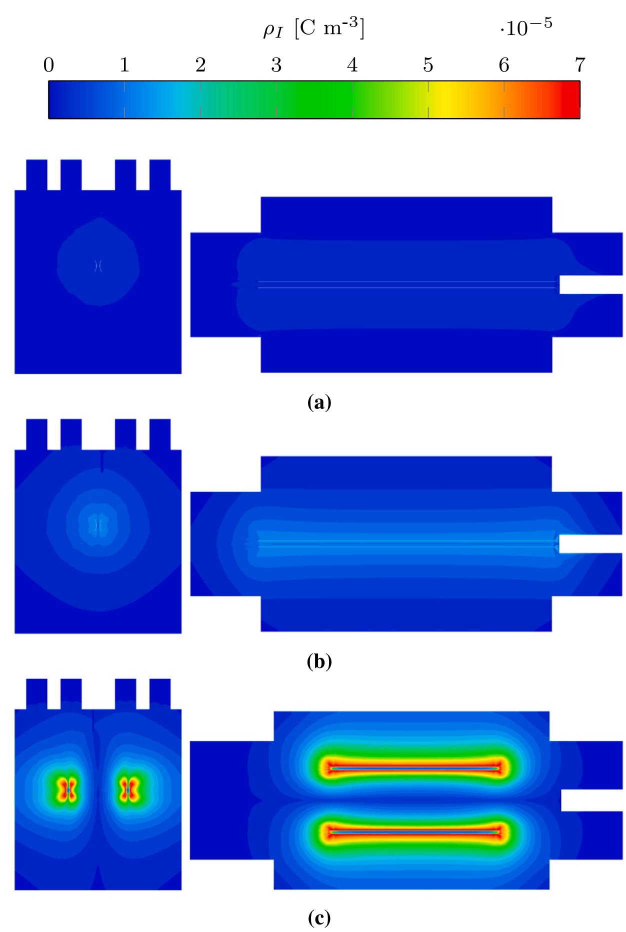

Fig. 7. Calculated ion space charge density around the discharge electrode for the different variants (Var1 to Var3, a to c). Left: front view, right: top view.

ion charge density not only occurs as a source term in the momentum conservation equation of the gas flow, but also influences the process of particle charging and thus the trajectories of the tracked particles. Fig. 7 shows the spatial distribution of ρ_I around the discharge electrodes of the three variants (Var1 to Var3). As can be clearly seen in the contour plots, constant and stable conditions arise due to the neglected diffusion term in the charge conservation equation and the associated dominance of the electric field on ρ_I. Basically, the ion space charge density, starting from the surface of the discharge electrode, decreases with increasing distance in the radial direction and is finally close to zero at the boiler wall. This pattern is least pronounced in variant 1, where the ion charge density around the cylindrical discharge wire is about $3.73 \cdot 10^{-6}\,\mathrm{C\,m^{-3}}$ due to the electrode geometry and the lower voltage of $22.8\,\mathrm{kV}$ compared to the other variants. With unchanged electrode geometry and an increase of the high voltage to approximately $28.0\,\mathrm{kV}$ (variant 2), this value can be increased by a factor of 4. Nevertheless, the radial progression of the space charge density decays quickly due to the central position of the discharge electrode and the associated release of free charge carriers. For this reason, the use of a single discharge electrode is not considered anymore and the concept of two parallel charge sources is pursued. The result of this development is represented by variant 3, where the discharge electrode is doubled and shortened in length, but nevertheless the electrode surface is enlarged. On the one hand, this avoids unwanted spark discharges to the back side wall of the boiler, and on the other hand it also achieves a superposition of the electrostatic field. The influence of this overlapping electrostatic fields is illustrated by the considerably higher space charge density on the discharge wires of about $7.27 \cdot 10^{-5}\,\mathrm{C\,m^{-3}}$ per electrode. Comparing this value with the two previous variants, an increase of ρ_I by a factor of 4.8 and 19.5 is obtained, respectively.

3.1.3. Particle tracking

In order to analyse the effects of the electrostatic field forces on the particle trajectories, a certain number of inert mono-disperse particles with different diameters (ranging from 0.025 to $25\,\mu\mathrm{m}$) are seeded equally distributed at the inlet face and tracked as they pass through the frozen flow field until they exit at the heat exchanger outlet. It is assumed that all injected particles have the same velocity as the entering flue gas stream. While those particles that come into contact with the surface of the collection electrode are considered to be deposited, those that collide with other surfaces (e. g. insulator) are reflected. Fig. 8 shows the trajectories of the salt particles with a diameter of 0.025 to $5.657\,\mu\mathrm{m}$ around the spray electrode positioned in the reversing chamber. It can be seen from the velocities that the particles are first slowed down due to the loss of momentum as they enter the reversing chamber. As they flow past the discharge electrodes, the particles are then charged. The resulting potential difference between the particles and the grounded boiler walls causes the particles to be accelerated towards the collection electrodes and subsequently be removed from the flue gas. Observing the trajectories in variant 1 (Fig. 8, a), it is evident that a large proportion of the particles follow the broadly formed vortex roller without action and thus quickly leave the reversing chamber. Due to the limited operating radius of the single discharge electrode, many particles are either insufficiently charged or not charged at all and can thus leave the exhaust system unimpeded. In contrast, with the particle movement around the double discharge electrode (Fig. 8, b), it is evident that the enlarged charging zone and the associated increased ion space charge density enable a much more efficient charging of the incoming particles. The dust particles thus do not follow the large vortex roller, but remain trapped for a longer time in smaller eddies around the discharge electrode. Those retained electrostatically charged particles are then mostly collected on the metal surfaces of the boiler.

Now, the separation performance for the different ESP variants can be evaluated based on the results of the particle tracking. As in the subsequent measurements, the collection efficiency $\eta(d_P)$ is used as the

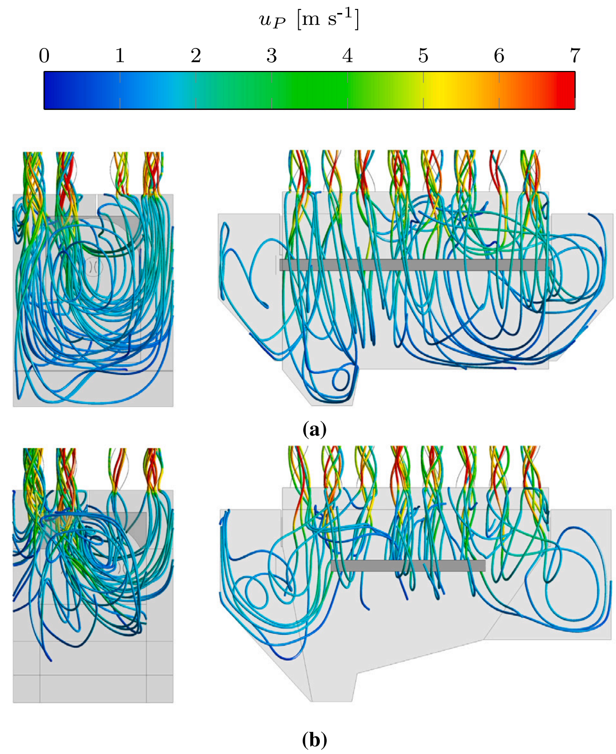

Fig. 8. Calculated course of particle trajectories (salt) around the discharge electrode for the single (Var2, a) and the double electrode (Var3, b). left: front view, right: side view.

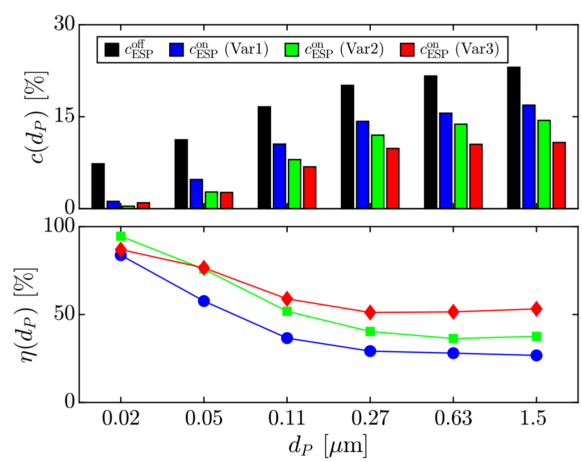

Fig. 9. Comparison of the calculated PM mass fraction at the heat exchanger inlet $c_{\mathrm{ESP}}^{\mathrm{off}}$ in and at the heat exchanger outlet $c_{\mathrm{ESP}}^{\mathrm{on}}$ for the different variants depending on the particle diameter. The resulting collection efficiency is determined according to the relationship $\eta\left(d_P\right) = 1 - c_{\mathrm{ESP}}^{\mathrm{on}}/c_{\mathrm{ESP}}^{\mathrm{off}}$.

decisive key indicator and can be calculated for each particle diameter by dividing the number of particles collected during the flow through the boiler with the number of particles injected at the heat exchanger inlet. Fig. 9 shows the collection efficiencies for the fine dust range ($d_P \le 1.5\,\mu\mathrm{m}$) determined with the help of the CFD simulation, as well as the mass fractions in the flue gas and purified gas. As can be seen from the bar chart, the mass fraction of particles with $d_P \ge 0.27\,\mu\mathrm{m}$ can be reduced from about 21.6 to 15.5% when using the first variant consisting of the single electrode. This corresponds to an average collection efficiency of about 28.0%. A change in the discharge electrode geometry (double electrode, Var3) and an increase in the applied voltage result in an improvement of the collection efficiency in this particle size range to an average of 38.1 and 52.0%, respectively. The collection efficiencies for all variants increase continuously with decreasing particle diameter ($d_P < 0.27\,\mu m$), but without any notable differences between the individual variants (Var2 and Var3). For particles with $d_P \geq 1.27\,\mu m$, variant 3 still shows a significantly better collection performance than the previous variant 2 ($\Delta\eta_{III-II} = 13.9\%$), while the differences in collection efficiency decrease to 7.1% for $d_P = 0.11\,\mu m$ and to less than 1% for $d_P < 0.05\,\mu m$. For very small particles ($d_P < 0.02\,\mu m$), the second variant even shows a slightly higher degree of separation. Furthermore, the separation efficiency of the first variant to some degree approaches that of the two high-voltage configurations with decreasing diameter. As the results of the simulations show, a significant improvement in the collection efficiency is achieved with each iteration step in the development process of the integrated ESP without constructing a prototype and spending a considerable amount of time testing it.

3.2. Experimental results

Aerosol measurements during the experimental boiler operation were carried out in accordance with the aerosol measuring techniques in the horizontal flue gas duct after the boiler, as explained in Section 2.4. However, the measurements could not be carried out simultaneously, as there was no corresponding sampling possibility on the flue gas flow before the integrated ESP. Hence, the dust measurements were carried out successively in chronological order, whereby the voltage of the discharge electrode is alternately switched on and off. The collection efficiency $\eta(d_P)$ of the integrated ESP was therefore determined indirectly via the PM concentration $c(d_P)$ of the respective particle fraction according to Eq. (12).

$$\eta(d_P) = 1 - \frac{c_{ESP}^{on}(d_P)}{c_{ESP}^{off}(d_P)} \tag{12}$$

As can be seen from the definition equation, results with different depth of information regarding the particle size d_P are available due to different measuring methods. While the test runs with varying biogenic fuels show the versatile application of the separator concept, the measurements with finer resolution of the particle size distribution allow a deeper insight into the separation characteristics of the individual aerosol fractions as well as an estimation of the health and environmental impacts, respectively.

3.2.1. Discontinuous PM measurements

The results of the discontinuous gravimetric PM measurements are listed in Table 4 for a total of four different biogenic fuels and two boiler load ranges. In addition to the combustion conditions, which are represented by the oxygen level for instance, the measured $PM_{2.5}$ emissions with and without the ESP as well as the collection efficiencies are shown. In the course of evaluating the different fuels, each load condition was measured three times with and without ESP. The results were then averaged to exclude outliers.

The first tests of the ESP were carried out with conventional wood pellets as a fuel. The data indicates typical combustion conditions characterised by low carbon monoxide ($y_{CO} \leq 3\,mg\,m_N^{-3}$) and nitrogen oxide ($y_{NO_x} = 67$ to $85\,mg\,m_N^{-3}$) emissions. The $PM_{2.5}$ emissions, which were measured with inactive ESP, can be quantified as 22.9 and $10.9\,mg\,m_N^{-3}$ under partial (PL) and nominal load (NL), respectively. With active ESP, the particle concentrations were reduced to 5.7 (PL) and $4.6\,mg\,m_N^{-3}$ (NL). This results in a collection efficiency for the $PM_{2.5}$ fraction of 57.2% in nominal furnace operation, while a significantly higher separation rate of about 74.6% can be achieved at reduced thermal load. The electrical power consumed by the ESP varies between 4 and 30 W depending on the load.

Furthermore, tests with wood chips were carried out, where two different fuel moisture contents ($w = 20$ and 40%) were examined. A first look at the gaseous emissions shows that there are much higher CO and NO_x emissions compared to the tests with pellets. The CO concentrations are between 69 and $234\,mg\,m_N^{-3}$, depending on load condition and fuel moisture, while the release of NO_x is just slightly higher with $114\,mg\,m_N^{-3}$ on average. In PL operation the combustion of dry wood chips (w20) causes a $PM_{2.5}$ content of about $43.5\,mg\,m_N^{-3}$ with the ESP switched off, while in NL operation $31.5\,mg\,m_N^{-3}$ are emitted. Although these raw gas loads are significantly higher than in the combustion tests with pellets, the collection efficiency hardly differ. The slightly lower collection efficiencies (50.1 and 72.2%) are also noticeable in the operation behaviour of the ESP. An electric current that is about 40% lower during the PL wood chips combustion at an almost identical voltage of approximately 37.7 kV reduces the supplied electrical power to just under 18 W. Turning now to the experiments with the wet wood chips (w40), clear differences in the emission behaviour of the firing system can be determined. With regard to particle emissions, it must be noted that the $PM_{2.5}$ concentrations in the untreated flue gas, which vary between 19.2 (PL) and $28.5\,mg\,m_N^{-3}$ (NL), are probably too low, since gas temperatures at the sampling point (not shown) were significantly lower than for the other measurements. The resulting uncontrolled condensation of the water vapour in the exhaust gas captures parts of the dust fraction, resulting in a lower measured value than expected. Despite such uncertainties in the PM measurements, the collection efficiencies are still calculated by assuming equal combustion conditions between tests with ESP switched on and off, respectively. The $PM_{2.5}$ concentrations decrease during ESP operation to around 6.8 (PL) and $13.2\,mg\,m_N^{-3}$ (NL) respectively, and are thus lower than expected, similar to the results with inactive ESP. The collection efficiencies calculated on the basis of the measured values are the lowest values of the examined fuels at 64.9 and 53.6%, respectively. Nevertheless, the good performance of the separator with regard to its operating point suggests that a positive effect is still given by the implementation of the ESP. This is supported by one of the highest measured values for the electrical power of the ESP in PL of about 25 W.

Finally, experiments with an alternative biogenic fuel were carried out. In this case, press residues from olive oil production are used. The fuel analysis attached in Appendix showed that the olive stones have similar properties in terms of bulk density, calorific value, water content and elementary composition compared to wood pellets. Hence, similar thermal outputs of approximately 34 and 99 kW were observed. However, fluctuations in combustion conditions, especially in the partial load phase, occur more frequently despite the fuel similarity. Nevertheless, stationary operating conditions could be sustained even when standard controller settings (pellets) were selected. The low CO emissions ($y_{CO} \approx 5\,mg\,m_N^{-3}$) at full load indicate nearly complete gas phase combustion conditions. In part load operation, the CO concentrations increase substantially, to almost $1000\,mg\,m_N^{-3}$. This in turn can be attributed to the aforementioned operating fluctuations. The formed NO_x compounds take up approximately 89 and $105\,mg\,m_N^{-3}$ respectively and are within the range of the previous tests with conventional biomass. In contrast to the gaseous emissions, comparatively high values are found for the $PM_{2.5}$ emissions with ESP switched off. Depending on the thermal power output, they can be quantified at around 85.5 (PL) and $80.4\,mg\,m_N^{-3}$ (NL). One reason for the high aerosol emissions may be coarse particles that were entrained with the primary air form the fuel bed. With active ESP, a $PM_{2.5}$ concentration of 14.0 (PL) and $25.5\,mg\,m_N^{-3}$ (NL) was observed, resulting in a reduction of submicron particles of 68.0 and 83.5%, respectively. Observing the operation conditions of the ESP, the highest voltage of all test arrangements was determined with about 39.5 kV in partial load operation of the plant. However, due to the low electric current ($I \approx 264\,\mu A$), this corresponded to a maximum power of only 10 W. A similar behaviour was noticed under nominal load, whereby a current half as high as during the pellet tests led to a minimum power of just over 2 W.

Table 4
Results of the discontinuous aerosol measurements ($PM_{2.5}$) and collection efficiency of the integrated ESP set-up (Var3) for different woody fuels and load cases of the biomass furnace (all emission measurement values refer to a dry base and a reference oxygen level of 13%; w20 and w40 refer to the moisture content of the wood chips).

Fuel	$\dot{Q}$ kW	u_{fg} m s^{-1}	T_{fg} °C	λ –	y_{O_2} %	y_{H_2O} %	y_{CO} mg m$_N^{-3}$	y_{NO_x} mg m$_N^{-3}$	y_{CH_4} mg m$_N^{-3}$	U_{ESP} kV	I_{ESP} µA	P_{ESP} W	c_{ESP}^{off} mg m$_N^{-3}$	c_{ESP}^{on} mg m$_N^{-3}$	η %
Pellets	36	1.2	111	2.2	12.2	8.1	107	67	0.7	37.8	795	30	22.6	5.7	74.6
	93	2.5	146	1.5	7.3	11.0	2	85	3.7	25.3	151	4	10.9	4.6	57.2
Wood chips (w20)	32	1.3	102	2.0	11.4	8.6	234	110	3.5	37.7	475	18	43.5	12.0	72.2
	104	3.2	187	1.4	6.7	11.8	69	115	25.8	23.0	307	7	31.5	15.7	50.1
Wood chips (w40)	39	0.9	103	1.7	9.7	13.1	151	131	2.4	39.1	633	25	19.2	6.8	64.9
	85	3.2	170	1.5	8.2	14.6	199	100	13.7	23.3	230	6	28.5	13.2	53.6
Olive stones	34	0.9	104	2.3	12.8	8.2	987	89	0.7	39.5	264	10	85.5	14.0	83.5
	99	2.4	158	1.3	6.1	11.7	5	105	0.6	27.8	86	3	80.4	25.5	68.0

3.2.2. Continuous PM measurements

In addition to the gravimetric dust measurements discussed in the previous section, further experiments were performed using continuous aerosol measurement techniques. Moreover, this section contains the results of the DGI measurements, which are needed for the calibration of the ELPI signal, as well as the concentration of the total suspended particles (TSP). As before, this test arrangement is divided into partial and nominal load phases of the furnace. Only a selected woody fuel was measured (wood chips w20). Fig. 10 illustrates combustion conditions during the aerosol measurements as well as the particle loads. A short interruption due to furnace cleaning is highlighted by the grey shaded areas, which required a restart in order to obtain the full measurement series. The corresponding distribution of the measured aerosol fraction as well as the collection efficiencies are shown in the two bottom graphs.

Looking first at the nominal load operating case of the furnace (Fig. 10, a), it can be observed that the maximum load value of around 80 mg m$_N^{-3}$ is present in the unpurified gas with a particle diameter of 5.15 µm. As the particle diameter decreases, the mass fraction in the flue gas reduces to below 40 mg m$_N^{-3}$, while the collection efficiency remains almost constant at about 39.5% down to a d_P of 1.99 µm. Although the larger particle fraction ($d_P \geq 1.99$ µm) accounts for about 59.1% of the mass-related dust emissions of the entire particle collective investigated, it must be pointed out that especially small respirable particles ($d_P \leq 1$ µm) are mainly responsible for health complaints. Turning now to only this area of the measured particle size distribution, it becomes apparent that significantly higher collection efficiencies are achieved for PM_1 and smaller particles, which may have a lower mass due to their small size. In the NL case of the furnace, the average collection efficiency for PM_1 was 54.3%. The distribution maximum of the measured aerosol fraction ($c(d_P) \approx 32$ mg m$_N^{-3}$) was present at a particle diameter of 0.21 µm, while the maximum collection efficiency of about 61.8% occurs with slightly larger particles. It is also shown that the integration of the ESP can reduce not only PM_1 emissions but also the release of total suspended particles by an average of 53.8%. With regard to the separator operation, it can be stated that an average voltage of approximately 23.1 kV can be maintained without frequent spark discharges and thus an average power of 7.4 W is introduced.

In addition to the measurements in nominal operation, the impact of the ESP on the PM emissions in partial load operation of the boiler is also investigated using ELPI measurement techniques (see Fig. 10, b). Although lower concentrations tend to occur in PL, the results of the PM emissions show similar proportions to those previously obtained in the NL measurements. As shown on the bottom right, the highest dust load occurs again with large particles ($d_P = 5.15$ µm) and is only half as high as in NL operation at approximately 43 mg m$_N^{-3}$. Despite the slightly lower dust concentrations, significantly higher collection efficiencies can be achieved in the PL range, whereby the general relationship with the particle diameter is also present here. The collection efficiency increases steadily as the particles become smaller after an initial constant value of 69.8% between 1.99 and 5.15 µm. With the start of the PM_1 fraction, the efficiency of the ESP is already clearly above 75% and consequently almost 30% higher than in the NL operation mode of the furnace. However, the distribution maximum of the aerosol fraction is not as clearly pronounced as in the NL phase. This peak is located somewhere between 0.21 and 0.32 µm and can be quantified as approximately 20.9 mg m$_N^{-3}$ for the untreated flue gas stream. With active ESP, this value is reduced by almost 14.1 mg m$_N^{-3}$ resulting in a maximum collection efficiency of 84.9% for PL operation. In contrast to NL, where the collection efficiency drops significantly towards the lower size range ($\eta \approx 45.8\%$ for $d_P = 0.13$ µm), the ESP efficiency stayed above 80% in PL operation. The total suspended particle emissions were reduced by an average of 66.4% through the use of the ESP. During operation, the ESP was kept at an average voltage of about 37.5 kV and an electrical power input of 27.8 W, respectively.

4. Conclusions

This study shows that the retrospective implementation of an electrostatic precipitator in a small biomass combustion system can certainly reduce the emission of particulate matter. Initial numerical simulations allow an insight into the complex processes of particle movement in an electrostatic field and thus enable the visualisation of optimisation measures with regard to the precipitator design (e. g. discharge electrode design) as well as to the fluid flow. Although CFD simulations cannot replace traditional experimental development steps, they significantly accelerate the development process and thus create the basis for the construction of already optimised prototypes.

As can be seen from the results of subsequent measurements, the proposed separator setup is especially efficient at collecting small particles ($PM_{2.5}$) from the flue gas with an efficiency of at least 55%. Depending on the fuel type of woody fuel and load condition of the furnace, the collection efficiency varies, with better particle separation at partial load due to lower gas temperatures and flow velocities ($\eta \approx$ 75%). Measurements with higher resolution of the particle size distribution (between 0.13 and 1.26 µm) also shows, that smaller particles are separated more efficiently (up to 80%) in both nominal and part load operation. The results clearly illustrate the concept and the effect of an integrated ESP and justify its use, especially in view of the low energy demand for its operation. Nevertheless, due to the complex processes during biomass combustion and particle formation mechanisms, further experimental investigations are necessary. In particular, the question arises as to whether the formation of combustion particles in the lower reversing chamber is completed to a sufficient degree, as otherwise the market readiness for integrated ESP's in the boiler body is a long way off.

Acknowledgements

This work was funded by the "Austrian Climate and Energy Fund" and the "Austrian Research Funding Association (FFG)" under the scope of the energy research programme, 2nd call, grant number: # 853606. The authors want to thank the partners from the companies Binder Energietechnik GmbH, Herz Energietechnik GmbH and Vienna University of Technology for their cooperation in this project.

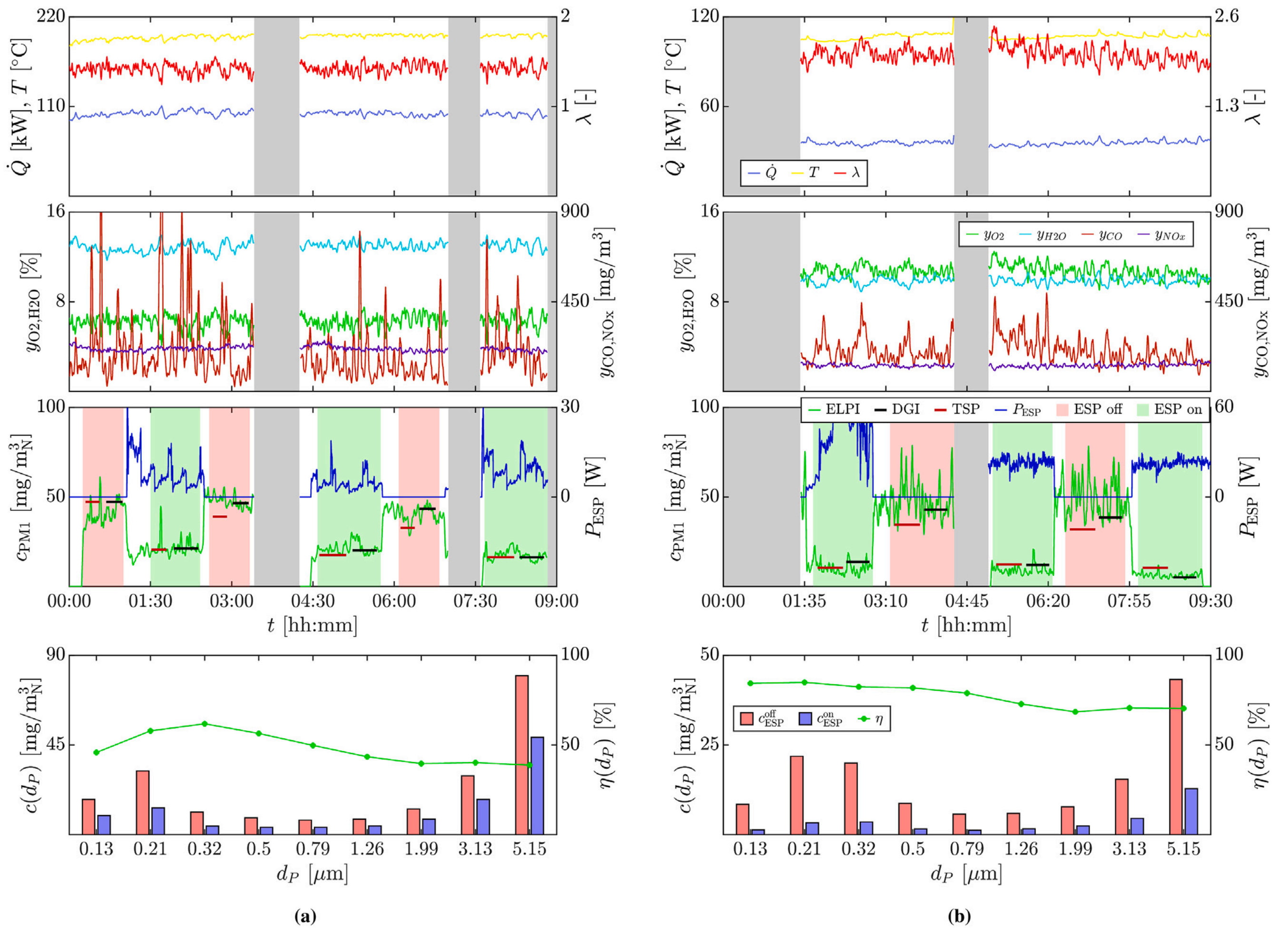

Fig. 10. Results of the ELPI, DGI and TSP measurements for the integrated ESP (Var3) during the combustion of dry wood chips (w20) for (a) nominal load and (b) partial load conditions.

Appendix. Fuel analysis

Table A.5 lists the results of the chemical analyses of the biogenic fuels burnt during the test runs. Since the measurement of the integrated ESP takes longer periods of time, multiple samples are taken to determine the fuel properties in order to take into account the inhomogeneity of the fuel. The final values are averaged from the individual samples.

The analysis results show that the fuels used hardly differ from each other in terms of ash content A_d and the main chemical constituents (C, H, N and O). Therefore, the lower and higher calorific value do not show any significant differences ($H_o \approx 20\,\mathrm{MJ\,kg_{db}^{-1}}$). The mass percentage of silicon (Si) and chlorine (Cl) is also in a similar range between 37 and $118\,\mathrm{mg\,kg_{db}^{-1}}$ for all fuels, with olive stones showing a slightly higher Cl content. The molar ratio Cl/Si, which indicates an increased release of potassium (K) from the fuel into the gas phase, reaches the maximum value of about 3.92 for the alternative fuel (olive stones). Consequently, high PM_1 emissions and thus deposits on the heat exchanger surfaces can be expected during the combustion of olive press residues. The three conventional biogenic fuels also have higher concentrations of ash-forming elements (Ca, Si, Mg and Na) than olive stones. It is also found that K is the most concentrated aerosol-forming element of all fuels investigated. According to this, the K content of olive residues is 2 to 3 times higher than that of woody biomass. The remaining aerosol-forming elements (Na, Zn and Pb) show significantly

Table A.5
Chemical characterisation of the biogenic fuels.

Quantity	Unit	Fuel type: Pellets	Wood chips w20	Wood chips w40	Olive stones
A_d	$\%_{db}$	0.40	0.66	0.53	0.44
w	$\%_{wb}$	7.1	19.1	39.3	5.9
C	$\%_{db}$	50.3	50.1	50.3	51.0
H	$\%_{db}$	5.97	5.95	5.99	5.80
N	$\%_{db}$	<0.10	0.11	<0.10	0.13
O	$\%_{db}$	43.5	43.5	43.5	42.8
S	$\mathrm{mg\,kg_{db}^{-1}}$	129	104	70	93
Cl	$\mathrm{mg\,kg_{db}^{-1}}$	75	68	91	118
Ca	$\mathrm{mg\,kg_{db}^{-1}}$	1070	1480	1320	323
Si	$\mathrm{mg\,kg_{db}^{-1}}$	53	92	37	38
Mg	$\mathrm{mg\,kg_{db}^{-1}}$	134	240	211	41
K	$\mathrm{mg\,kg_{db}^{-1}}$	409	770	698	1670
Na	$\mathrm{mg\,kg_{db}^{-1}}$	12	11	13	10
Pb	$\mathrm{mg\,kg_{db}^{-1}}$	2	3	3	3
Zn	$\mathrm{mg\,kg_{db}^{-1}}$	10	13	19	3
H_u	$\mathrm{MJ\,kg_{db}^{-1}}$	18.79	18.81	18.82	19.10
H_o	$\mathrm{MJ\,kg_{db}^{-1}}$	20.10	20.12	20.14	20.37

lower concentrations compared to K and are at similar levels for all biogenic fuels used.

References

[1] A. Welfle, P. Gilbert, P. Thornley, A. Stephenson, Generating low-carbon heat from biomass: Life cycle assessment of bioenergy scenarios, J. Clean. Prod. 149 (2017) 448–460, http://dx.doi.org/10.1016/j.jclepro.2017.02.035.

[2] E.O. Jåstad, T.F. Bolkesjø, E. Trømborg, P.K. Rørstad, The role of woody biomass for reduction of fossil GHG emissions in the future north European energy sector, Appl. Energy 274 (2020) 115360, http://dx.doi.org/10.1016/j.apenergy.2020.115360.

[3] L.S. Johansson, B. Leckner, L. Gustavsson, D. Cooper, C. Tullin, A. Potter, Emission characteristics of modern and old-type residential boilers fired with wood logs and wood pellets, Atmos. Environ. 38 (25) (2004) 4183–4195, http://dx.doi.org/10.1016/j.atmosenv.2004.04.020.

[4] J. Kelz, T. Brunner, I. Obernberger, P. Jalava, M.-R. Hirvonen, PM emissions from old and modern biomass combustion systems and their health effects, in: Proceedings of the 18th European Biomass Conference and Exhibition, ETA-Florence Renewable Energies, 2010, pp. 1231–1243, http://dx.doi.org/10.5071/18thEUBCE2010-OA11.5.

[5] C. Schmidl, M. Luisser, E. Padouvas, L. Lasselsberger, M. Rzaca, C. Ramirez-Santa Cruz, M. Handler, G. Peng, H. Bauer, H. Puxbaum, Particulate and gaseous emissions from manually and automatically fired small scale combustion systems, Atmos. Environ. 45 (39) (2011) 7443–7454, http://dx.doi.org/10.1016/j.atmosenv.2011.05.006.

[6] L.S. Bäfver, B. Leckner, C. Tullin, M. Berntsen, Particle emissions from pellets stoves and modern and old-type wood stoves, Biomass Bioenergy 35 (8) (2011) 3648–3655, http://dx.doi.org/10.1016/j.biombioe.2011.05.027.

[7] L. Lillieblad, A. Szpila, M. Strand, J. Pagels, K. Rupar-Gadd, A. Gudmundsson, E. Swietlicki, M. Bohgard, M. Sanati, Boiler operation influence on the emissions of submicrometer-sized particles and polycyclic aromatic hydrocarbons from biomass-fired grate boilers, Energy Fuels 18 (2) (2004) 410–417, http://dx.doi.org/10.1021/ef0300444.

[8] W.J. Smith, S. Morrin, D.J. Timoney, Effect of operating condition on the particulate matter emission factor for a domestic biomass boiler, Proc. Inst. Mech. Eng. Part A J. Power Energy 225 (5) (2011) 614–618, http://dx.doi.org/10.1177/0957650911399827.

[9] R. Nyström, R. Lindgren, R. Avagyan, R. Westerholm, S. Lundstedt, C. Boman, Influence of wood species and burning conditions on particle emission characteristics in a residential wood stove, Energy Fuels 31 (5) (2017) 5514–5524, http://dx.doi.org/10.1021/acs.energyfuels.6b02751.

[10] H. Wiinikka, R. Gebart, The influence of fuel type on particle emissions in combustion of biomass pellets, Combust. Sci. Technol. 177 (4) (2005) 741–763, http://dx.doi.org/10.1080/00102200590917257.

[11] J. Kelz, C. Zemann, D. Muschick, O. Krenn, G. Hofmeister, A. Weissinger, M. Gölles, C. Hochenauer, Evaluation of the combustion behaviour of straw, poplar and maize in a small-scale biomass boiler, in: Proceedings of the 25th European Biomass Conference and Exhibition, ETA-Florence Renewable Energies, 2017, pp. 1958–1966, http://dx.doi.org/10.5071/25thEUBCE2017-ICO.12.5.

[12] J.O. Anderson, J.G. Thundiyil, A. Stolbach, Clearing the air: a review of the effects of particulate matter air pollution on human health, J. Med. Toxicol. 8 (2) (2012) 166–175, http://dx.doi.org/10.1007/s13181-011-0203-1, arXiv:22194192.

[13] World Health Organization, Health Effects of Particulate Matter, World Health Organization, 2013.

[14] T. Nussbaumer, Aerosols from Biomass Combustion, IEA Bioenergy, 2017.

[15] The Swiss Federal Council, Ordinance on air pollution control (luftreinhalte verordnung), 1985.

[16] Federal Ministry for the Environment, Nature Conservation and Nuclear Safety of Germany, First ordinance on the implementation of the federal immission control act (ordinance on small and medium-sized firing installations), 2010.

[17] A. Jaworek, A. Krupa, T. Czech, Modern electrostatic devices and methods for exhaust gas cleaning: A brief review, J. Electrostat. 65 (3) (2007) 133–155, http://dx.doi.org/10.1016/j.elstat.2006.07.012.

[18] A. Jaworek, A.T. Sobczyk, A. Marchewicz, A. Krupa, T. Czech, Particulate matter emission control from small residential boilers after biomass combustion. a review, Renew. Sust. Energy Rev. (2020) 110446, http://dx.doi.org/10.1016/j.rser.2020.110446.

[19] C. Mandl, I. Obernberger, F. Biedermann, State-of-the-art and assessment of filter technologies for residential biomass combustion systems, in: Proceedings of the 20th European Biomass Conference and Exhibition, ETA-Florence Renewable Energies, 2012, pp. 732–738, http://dx.doi.org/10.5071/20thEUBCE2012-2BO.4.4.

[20] Z. Ning, J. Podlinski, X. Shen, S. Li, S. Wang, P. Han, K. Yan, Electrode geometry optimization in wire-plate electrostatic precipitator and its impact on collection efficiency, J. Electrostat. 80 (2016) 76–84, http://dx.doi.org/10.1016/j.elstat.2016.02.001.

[21] F. Miloua, A. Tilmatine, R. Gouri, N. Kadous, L. Dascalescu, Optimization of the rapping process of an intermittent electrostatic precipitator, Eur. Phys. J. Appl. Phys. 41 (1) (2008) 81–85, http://dx.doi.org/10.1051/epjap:2007175.

[22] S.L. Francis, A. Bäck, P. Johansson, Reduction of rapping losses to improve ESP performance, in: K. Yan (Ed.), Electrostatic Precipitation, Springer-Verlag Berlin Heidelberg, 2009, pp. 45–49.

[23] V. Schmatloch, S. Rauch, Design and characterisation of an electrostatic precipitator for small heating appliances, J. Electrostat. 63 (2) (2005) 85–100, http://dx.doi.org/10.1016/j.elstat.2004.08.001.

[24] A. Bologa, H.R. Paur, K. Woletz, Development and study of an electrostatic precipitator for small scale wood combustion, Int. J. Plasma Environ. Sci. Technol. 5 (2) (2011) 168–173, http://dx.doi.org/10.34343/ijpest.2011.05.02.168.

[25] J. Carroll, J. Finnan, Use of electrostatic precipitators in small-scale biomass furnaces to reduce particulate emissions from a range of feedstocks, Biosyst. Eng. 163 (2017) 94–102, http://dx.doi.org/10.1016/j.biosystemseng.2017.08.021.

[26] J. Oischinger, M. Steiner, M. Meiller, M. Hebauer, S. Beer, R. Daschner, A. Hornung, J. Kramb, Optimization of the fractional collection efficiencies for electrostatic precipitators used in biomass-fired boilers, Biomass Bioenergy 141 (11) (2020) 105703, http://dx.doi.org/10.1016/j.biombioe.2020.105703.

[27] A. Berhardt, F. Lezsovits, B. Groß, Integrated electrostatic precipitator for small-scaled biomass boilers, Chem. Eng. Technol. 40 (2) (2017) 278–288, http://dx.doi.org/10.1002/ceat.201600200.

[28] J. Kelz, C. Zemann, D. Muschick, G. Hofmeister, M. Gölles, S. Retschitzegger, Performance evaluation of an electrostatic precipitator in a small-scale biomass boiler by using different biomass feedstocks, in: Proceedings of the 27th European Biomass Conference and Exhibition, ETA-Florence Renewable Energies, 2019, pp. 1932–1938, http://dx.doi.org/10.5071/27thEUBCE2019-IBV.1.20.

[29] O. Molchanov, K. Krpec, J. Horák, Electrostatic precipitation as a method to control the emissions of particulate matter from small-scale combustion units, J. Clean. Prod. 246 (2020) 119022, http://dx.doi.org/10.1016/j.jclepro.2019.119022.

[30] M. Blank, M. Schöffl, R. Scharler, I. Obernberger, New CFD based model for the design and optimisation of electrostatic precipitators for biomass combustion plants, in: Proceedings of the 23rd European Biomass Conference and Exhibition, ETA-Florence Renewable Energies, 2015, pp. 540–545, http://dx.doi.org/10.5071/23rdEUBCE2015-2BO.4.5.

[31] K. Nikas, A.A. Varonos, G.C. Bergeles, Numerical simulation of the flow and the collection mechanisms inside a laboratory scale electrostatic precipitator, J. Electrostat. 63 (5) (2005) 423–443, http://dx.doi.org/10.1016/j.elstat.2004.12.005.

[32] N. Farnoosh, K. Adamiak, G. Castle, 3-D numerical analysis of EHD turbulent flow and mono-disperse charged particle transport and collection in a wire-plate ESP, J. Electrostat. 68 (6) (2010) 513–522, http://dx.doi.org/10.1016/j.elstat.2010.07.002.

[33] B. Guo, A. Yu, J. Guo, Numerical modelling of ESP for design optimization, Procedia Eng. 102 (2015) 1366–1372, http://dx.doi.org/10.1016/j.proeng.2015.01.268.

[34] J.-W. Park, C. Kim, J. Park, J. Hwang, Computational fluid dynamic modelling of particle charging and collection in a wire-to-plate type single-stage electrostatic precipitator, Aerosol Air Qual. Res. 18 (3) (2018) 590–601, http://dx.doi.org/10.4209/aaqr.2017.05.0176.

[35] G. Skodras, S.P. Kaldis, D. Sofialidis, O. Faltsi, P. Grammelis, G.P. Sakellaropoulos, Particulate removal via electrostatic precipitators — CFD simulation, Fuel Process. Technol. 87 (7) (2006) 623–631, http://dx.doi.org/10.1016/j.fuproc.2006.01.012.

[36] K. Dastoori, B. Makin, M. Kolhe, M. Des-Roseaux, M. Conneely, CFD modelling of flue gas particulates in a biomass fired stove with electrostatic precipitation, J. Electrostat. 71 (3) (2013) 351–356, http://dx.doi.org/10.1016/j.elstat.2012.12.039.

[37] S. Arif, D.J. Branken, R.C. Everson, H. Neomagus, L.A. Le Grange, A. Arif, CFD modeling of particle charging and collection in electrostatic precipitators, J. Electrostat. 84 (2016) 10–22, http://dx.doi.org/10.1016/j.elstat.2016.08.008.

[38] C. Bhasker, Flow simulation in electro-static-precipitator (ESP) ducts with turning vanes, Adv. Eng. Softw. 42 (7) (2011) 501–512, http://dx.doi.org/10.1016/j.advengsoft.2011.04.002.

[39] T.-H. Shih, W.W. Liou, A. Shabbir, Z. Yang, J. Zhu, A new k-e eddy viscosity model for high reynolds number turbulent flows, Comput. Fluids 24 (3) (1995) 227–238, http://dx.doi.org/10.1016/0045-7930(94)00032-T.

[40] G. Kohnen, Über Den Einfluß Der Phasenwechselwirkungen Bei Turbulenten Zweiphasenströmungen Und Deren Numerische Erfassung in Der Euler-Lagrange-Betrachtungsweise, Berichte aus der Strömungstechnik, Shaker, 1997.

[41] R. Scharler, Entwicklung und optimierung von biomasse-rostfeuerungen durch CFD-analyse, TU Graz, 2001.

[42] S.V. Patankar, A calculation procedure for two-dimensional elliptic situations, Num. Heat Transf. 4 (4) (1981) 409–425, http://dx.doi.org/10.1080/01495728108961801.

[43] H.-J. Schmid, S. Stolz, H. Buggisch, On the modelling of the electro-hydrodynamic flow field in electrostatic precipitators, Flow Turbul. Combust. 68 (1) (2002) 63–89, http://dx.doi.org/10.1023/A:1015666116174.

[44] M. Horn, Zur Modellierung Partikulärer Elektro-Fluiddynamischer Strömungen, first ed., Cuvillier Verlag, 2010.
[45] H.-J. Schmid, L. Vogel, On the modelling of the particle dynamics in electro-hydrodynamic flow-fields: I. Comparison of Eulerian and Lagrangian modelling approach, Powder Technol. 135–136 (2003) 118–135, http://dx.doi.org/10.1016/j.powtec.2003.08.009.
[46] P.N. Rowe, G.A. Henwood, Drag forces in hydraulic model of a fluidized bed-part I, Trans. Inst. Chem. Eng. 39 (1962) 43–54.
[47] D.K. Hutchins, M.H. Harper, R.L. Felder, Slip correction measurements for solid spherical particles by modulated dynamic light scattering, Aerosol Sci. Tech. 22 (2) (1995) 202–218, http://dx.doi.org/10.1080/02786829408959741.
[48] Z. Long, Q. Yao, Evaluation of various particle charging models for simulating particle dynamics in electrostatic precipitators, J. Aerosol Sci. 41 (7) (2010) 702–718, http://dx.doi.org/10.1016/j.jaerosci.2010.04.005.
[49] P.A. Lawless, Particle charging bounds, symmetry relations, and an analytic charging rate model for the continuum regime, J. Aerosol Sci. 27 (2) (1996) 191–215, http://dx.doi.org/10.1016/0021-8502(95)00541-2.
[50] N. Neimarlija, I. Demirdžić, S. Muzaferija, Numerical method for calculation of two-phase electrohydrodynamic flows in electrostatic precipitators, Numer. Heat Tr. A-Appl. 59 (5) (2011) 321–348, http://dx.doi.org/10.1080/10407782.2011.549080.
[51] M. Schöffl, Entwicklung eines CFD-modells für die Simulation von Elektrofiltern für Biomasse-Feuerungsanlagen, TU Graz, 2014.
[52] C.-U. Böttner, Über den einfluss der elektrostatischen Feldkraft auf turbulente Zweiphasenströmungen, MLU, 2002.
[53] F.W. Peek, Dielectric Phenomena in High Voltage Engineering, McGraw-Hill Book Company, inc., 1929.
[54] J.S. Chang, C.A. McLinden, A.A. Berezin, P.C. Looy, Modelling of quadrupole cold precharger dust particle charging characteristics, in: Conference Record of the 1993 IEEE Industry Applications Conference, IEEE Industry Applications Society, IEEE, 1993, pp. 1851–1858, http://dx.doi.org/10.1109/IAS.1993.299102.
[55] VDI 2066 - Particulate matter measurement - Dust measurement in flowing gases - Gravimetric determination of dust load, 13.040.40, (VDI 2066).
[56] T. Schröder, J. von Sonntag, T. Ulbricht, P. Heidecke, E. Stahl, C. Schön, H. Hartmann, D. Kuptz, N. Woltersdorf, R. Kunde, M. Adeili, F. Volz, Methods for Measuring Emissions of Particulate Matter from Solid Biomass Combustion, Vol. 08, Deutsches Biomasseforschungszentrum gemeinnützige GmbH, 2018,
[57] A. Kather, N. Woltersdorf, Feinstaubemissionen aus biomassebefeuerten Kleinfeuerungsanlagen, TU Hamburg, Institut für Energietechnik, 2013.
[58] J. Keskinen, K. Pietarinen, M. Lehtimäki, Electrical low pressure impactor, J. Aerosol Sci. 23 (4) (1992) 353–360, http://dx.doi.org/10.1016/0021-8502(92)90004-F.
[59] M. Marjamäki, J. Keskinen, D.-R. Chen, D.Y. Pui, Performance evaluation of the electrical low-pressure impactor (ELPI), J. Aerosol Sci. 31 (2) (2000) 249–261, http://dx.doi.org/10.1016/S0021-8502(99)00052-X.
[60] R. Sh. Islamov, Influence of gas velocity on the particle collection and reentrainment in an air-cleaning electrostatic precipitator, Aerosol Sci. Tech. 52 (12) (2018) 1415–1428, http://dx.doi.org/10.1080/02786826.2018.1528003.
[61] K. Luo, Y. Li, C. Zheng, X. Gao, J. Fan, Numerical simulation of temperature effect on particles behavior via electrostatic precipitators, Appl. Therm. Eng. 88 (2015) 127–139, http://dx.doi.org/10.1016/j.applthermaleng.2014.11.078.